Geophysical Research Letters

RESEARCH LETTER
10.1029/2025GL117472

# Composite Three-Dimensional Biogeochemical Responses to Tropical Cyclones in the Northwest Pacific

**Hui Zheng**[1,2,3,4], **Wen-Zhou Zhang**[1,2,3,4], **and Zhiguo Mei**[1,2,3,4]

[1]College of Ocean and Earth Sciences, Fujian Provincial Key Laboratory for Coastal Ecology and Environmental Studies, Xiamen University, Xiamen, China, [2]State Key Laboratory of Marine Environmental Science, Xiamen University, Xiamen, China, [3]Coastal and Ocean Management Institute (COMI), Xiamen University, Xiamen, China, [4]Key Laboratory of Underwater Acoustic Communication and Marine Information Technology, Xiamen University, Ministry of Education, Xiamen, China

**Abstract** We innovatively investigated three-dimensional biogeochemical responses to tropical cyclones (TCs) in the Northwest Pacific using a composite analysis of simulations from a coupled physical-biogeochemical model. TC-induced upwelling and vertical mixing cause a vertical redistribution of chlorophyll *a* concentration (Chl-*a*), increasing surface Chl-*a* while decreasing subsurface Chl-*a*, within a 100-km radius of the TC center. Simultaneously, these processes bring nutrient-rich deep waters into the upper layer. Following the TC passage, the significant increases in both Chl-*a* and nutrients lead to a high Chl-*a* anomaly in the subsurface layer that persists for over 30 days. Westward geostrophic advection, driven by the meridional density gradient, tends to shift the subsurface nutrients and Chl-*a* anomalies toward the left side of the generally northwestward TC track. The total biomass in the upper ocean, as indicated by integrated Chl-*a*, decreases shortly after the TC passage and subsequently starts to rise, ultimately resulting in a net increase.

**Plain Language Summary** Using 18-years of simulation data from a coupled physical-biogeochemical model, we conducted the first three-dimensional composite analysis of upper ocean biogeochemical responses to tropical cyclones (TCs) in the Northwest Pacific. Generally, the vertical distribution of chlorophyll *a* concentration (Chl-*a*) is characterized by a deep Chl-*a* maximum in open oceans. TC-induced vertical mixing and upwelling lead to surface Chl-*a* increase and subsurface Chl-*a* decrease. Meanwhile, deep waters with high nutrients are uplifted into the upper layer. The strong biogeochemical responses to TCs mainly happen within a radius of 100 km from the TC track. With the TC influence, the temporal evolution of Chl-*a* varies with depth and high Chl-*a* anomalies in the subsurface layer persist for more than 30 days because both Chl-*a* and nutrients increase significantly after the TC passage. The subsurface nutrients and Chl-*a* anomalies gradually shift to the left side of the northwestward TC track due to the westward geostrophic advection caused by the northward density gradient in the upper ocean. The time series of integrated Chl-*a* indicates that the TC leads to a net increase in total biomass.

**Key Points:**

- The first 3D composite analysis of biogeochemical responses to tropical cyclones (TCs) in the Northwest Pacific was conducted based on model simulations
- Advection effect of background current results in a leftward-shifting feature of subsurface chlorophyll *a* and nitrate anomalies after TC passage
- TC could increase total biomass in general, although the total biomass decreases significantly in the first few days after the TC passage

**Supporting Information:**

Supporting Information may be found in the online version of this article.

**Correspondence to:**

W.-Z. Zhang,
zwenzhou@xmu.edu.cn

**Citation:**

Zheng, H., Zhang, W.-Z., & Mei, Z. (2025). Composite three-dimensional biogeochemical responses to tropical cyclones in the Northwest Pacific. *Geophysical Research Letters*, *52*, e2025GL117472. https://doi.org/10.1029/2025GL117472

Received 13 JUN 2025
Accepted 27 AUG 2025

**Author Contributions:**

**Conceptualization:** Wen-Zhou Zhang
**Data curation:** Hui Zheng
**Formal analysis:** Hui Zheng, Zhiguo Mei
**Funding acquisition:** Wen-Zhou Zhang
**Investigation:** Hui Zheng, Wen-Zhou Zhang
**Methodology:** Hui Zheng, Wen-Zhou Zhang, Zhiguo Mei
**Project administration:** Wen-Zhou Zhang
**Software:** Hui Zheng, Zhiguo Mei
**Supervision:** Wen-Zhou Zhang
**Validation:** Hui Zheng, Zhiguo Mei
**Visualization:** Hui Zheng
**Writing – original draft:** Hui Zheng



## 1. Introduction

Tropical cyclones (TCs) are among the most intense synoptic events, which induce upwelling, mixing, and entrainment due to strong cyclonic winds, resulting in a cold wake along TC tracks (Dickey et al., 1998; Price, 1981; Price et al., 1994). TCs not only change and induce the aforementioned dynamic processes but also temporarily regulate and alter biogeochemical cycles in the upper oceans, leading to change in ocean primary production which is critical for ocean ecosystem, air-sea carbon dioxide ($CO_2$) exchange and ocean carbon sequestration efficiency (Babin et al., 2004; I. Lin et al., 2003; Siswanto et al., 2009; Subrahmanyam et al., 2002). In the Northern (Southern) Hemisphere, on account of wind-current resonance, sea surface responses to a TC are stronger on the right (left) side of its track, looking in the TC moving direction (Dickey & Simpson, 1983; Price, 1981). In terms of TC frequency and intensity, the Northwest Pacific undergoes the greatest TC impacts in the world (Kossin et al., 2013; Webster et al., 2005).

Numerous remote sensing data suggest that TCs frequently cause an increase in surface chlorophyll *a* concentration (Chl-*a*) in oligotrophic oceans (Babin et al., 2004; Gierach & Subrahmanyam, 2008; Lin, 2012; Zhao & Wang, 2018), and the TC-induced surface Chl-*a* anomaly can last for more than 2 weeks (Jiang et al., 2023; Wang, 2020; Wang & Xiu, 2022). In general, strong and slow-moving TCs readily trigger sea surface phytoplankton blooms (Foltz et al., 2015; Hanshaw et al., 2008; Lin, 2012; Mei et al., 2015; Wang, 2020). Previous

**Writing – review & editing:** Wen-Zhou Zhang, Zhiguo Mei

studies demonstrated that compared with the intensity of a TC, the TC translation speed is more crucial for biogeochemical responses (J. Li et al., 2021; Sun et al., 2010; Zhao et al., 2008). Post-TC surface Chl-*a* is highly correlated with the time period when a TC moves slowly (translation speed <3 m/s), a "hover" parameter ( Russell & Horvat, 2023). In addition, the biogeochemical responses are also related to pre-TC ocean conditions. For instance, the surface Chl-*a* response largely depends on pre-TC mixed layer depth (MLD) (Jiang et al., 2023).

In the subsurface layer, biogeochemical responses to TCs are more complex compared with those in the surface layer. When the TC-induced physical processes just bring subsurface water with high Chl-*a* into the surface layer without significantly altering the vertical structures of nutrients, the surface (subsurface) Chl-*a* increases (decreases), resulting in negligible changes in the upper ocean depth integration of Chl-*a* (Chai et al., 2021). When the TC-induced upwelling and entrainment are strong enough to cause the outcrop of nutrients, the Chl-*a* in both surface and subsurface layers increases, indicating a net increase of primary production (Kao et al., 2023; I. Lin et al., 2003; Naik et al., 2008; Yu et al., 2022). Unlike those two situations, Ye et al. (2013) revealed that TC Nuri triggered a prominent subsurface Chl-*a* bloom, but little surface Chl-*a* increase. This is because the subsurface upwelling induced by Nuri brought much nutrient-rich deep water up to the euphotic layer without outcropping. A similar phenomenon was also found in numerical simulations (Pan et al., 2017).

To date, TC-induced biogeochemical responses have been investigated mainly through satellite data, on account of limited in situ observations. However, satellite-derived surface Chl-*a* is easily contaminated by clouds, particularly during the TC period. Results relying solely on satellite sensing data may overestimate and underestimate the effects of TCs on primary production in the upper ocean because of the aforementioned TC-induced Chl-*a* redistribution and subsurface Chl-*a* (phytoplankton) blooms, respectively (Zheng & Zhang, 2023). Although Biogeochemical-Argo (BGC-Argo) floats have been gradually applied to marine biogeochemical research in recent years (e.g., Cossarini et al., 2019; Wang et al., 2021), the number of BGC-Argo floats equipped with extensive biogeochemical sensors is still limited (Chai et al., 2020). Consequently, past research on the biogeochemical responses to TCs based on BGC-Argo float observations has focused on individual cases (Chacko, 2017; Chai et al., 2021; Qiu et al., 2021). Thus, the comprehensive impacts of TCs on biogeochemical processes and the ecological environment in the upper ocean, particularly in the subsurface layer, are still unclear.

Unlike conventional case studies and surface analyses of remote sensing data, numerical model simulations enable a 3D composite analysis of oceanic responses to TCs forcing. For the first time, this study employs simulation data from a coupled physical-biogeochemical model to conduct a composite analysis of three-dimensional (3D) biogeochemical changes induced by TCs that occurred in the Northwest Pacific between 2005 and 2022. Based on the composite analysis of model simulations for 226 TCs, we systematically quantify 3D changes in key biogeochemical parameters (Chl-*a* and nitrate) and the temporal evolution of total phytoplankton biomass in the upper ocean within TC influence areas in a statistical sense.

## 2. Data and Methods

### 2.1. Model and Its Validation

In this work, a coupled physical-biogeochemical model was developed, based on the Regional Ocean Modeling System (ROMS) (Shchepetkin & McWilliams, 2005) and the Carbon, Silicate, and Nitrogen Ecosystem (CoSiNE) model (Chai et al., 2002). Similar coupled models have been widely used to study ocean biogeochemical processes in the literature (Y. Li et al., 2022; Xiu & Chai, 2012; Zhou et al., 2017). The model domain covers most of the Northwest Pacific (99°–150°E, 15°S–41°N), where TCs frequently occur (Figure 1). The horizontal resolution is 1/20° in both longitude and latitude, and there are 50 terrain-following layers in the vertical. The minimum and maximum depths of this model are 5 and 5,000 m, respectively.

In the model, the initial and boundary states for physical components were taken from the World Ocean Atlas 2018 (WOA18) (Garcia et al., 2019) and the global ocean eddy-resolving reanalysis (GLORYS12V1) provided by Copernicus Marine Service Information (CMEMS) of Mercator Ocean (Lellouche et al., 2018), respectively. As for biogeochemical components, the initial and boundary data were obtained from the outputs of the CoSiNE-Pacific model (Xiu et al., 2010). The runoff data were provided by the Chinese River Sediment Bulletin and A. Dai (2017). Tidal forcing was also considered in this model, using 15 tidal components taken from the results of the TPXO9 tidal model (Egbert & Erofeeva, 2002). Surface atmospheric forcing data were derived from the fifth generation European Centre for Medium-Range Weather Forecasts (ECMWF) reanalysis (ERA5) data set

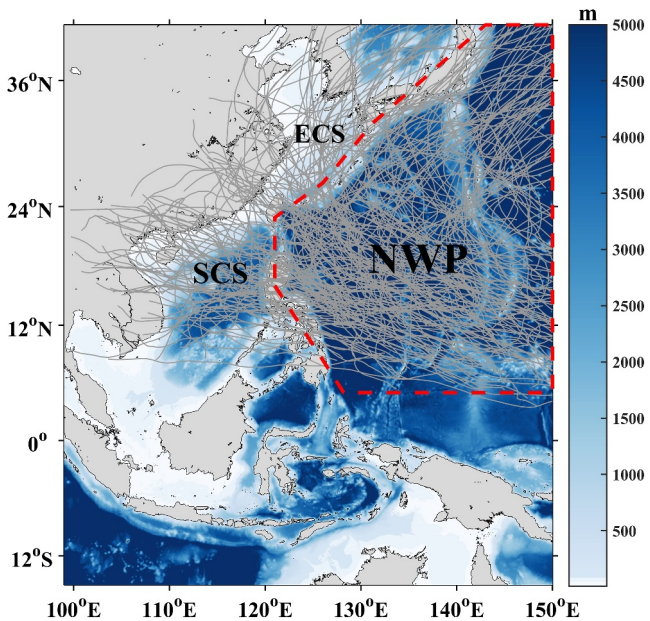


**Figure 1.** The model domain and bathymetry in meters (color shading). Gray solid lines represent the tracks of all tropical cyclones with Saffir-Simpson category ≥1 from 2005 to 2022. The area surrounded by red dashed lines denotes the study area. NWP, Northwest Pacific; SCS, South China Sea; ECS, East China Sea.

(Hersbach et al., 2023). Note that ERA5 winds near the eye-wall are much weaker than corresponding data from the International Best Track Archive for Climate Stewardship (IBTrACS) data set (Gahtan et al., 2024). To ensure the accuracy of TC intensity in the model simulation, a TC wind fusion method was applied for ERA5 wind correction following Sun et al. (2015). This ROMS-CoSiNE coupled model was run for the 29-year period from 1994 to 2022, and the results from 2005 to 2022 were used for analysis in this study due to the lack of sufficient data for wind field fusion before 2005.

For model validation, multiple satellite data were applied in this study. Daily sea surface temperature (SST) and monthly sea surface salinity (SSS) data were taken from the microwave and infrared Optimally Interpolated SST (MW_IR OI SST) daily products (Remote Sensing Systems, 2022) and Soil Moisture Active Passive (SMAP) SSS V6.0 (Meissner et al., 2024), respectively. Surface Chl-*a* data were obtained from the Moderate Resolution Imaging Spectroradiometer (MODIS) level-3 products (NASA Ocean Biology Processing Group, 2014). In addition, extensive in situ observation profiles were also used to evaluate the model performance in the upper ocean. More than 120,000 vertical temperature and salinity profiles were collected from Argo floats. The numbers of Chl-*a* and nitrate profiles extracted from BGC-Argo floats and the World Ocean Database were 4,903 and 3,966, respectively. The locations of in situ observation profiles for model validation are showed in Figure S1 in Supporting Information S1.

The comparison of model temperature results with observed data (Figure S2 in Supporting Information S1) shows that although the model SST is slightly higher than OI SST (about 0.4°C), the seasonal and interannual variations of model SST are in good agreement with OI SST. Besides, we used the structural similarity index (SSIM) (Wang et al., 2004) as a proxy for the similarity in spatial pattern between the model SST and OI SST. The results indicate that the horizontal distribution of model SST matches OI SST well throughout the study period with a mean SSIM of 0.8. Further, the model outputs were compared with the temperature profiles from Argo floats (Argo, 2000) at the same date and location, demonstrating almost no difference in mean vertical temperature structure. The model SSS is approximately 0.3 psu higher than SMAP observations. This discrepancy is likely because the model incorporates only 18 rivers, resulting in weaker terrestrial freshwater input than reality. Nevertheless, the spatial and temporal variations of model SSS are consistent with SMAP. Furthermore, the model salinity below the surface layer closely matches the Argo float observations, particularly below 200 m depth (Figure S3 in Supporting Information S1). As for surface Chl-*a*, although the model surface Chl-*a* is slightly lower than MODIS (Figure S4 in Supporting Information S1), the model results and satellite data have similar spatiotemporal characteristics, like SST and SSS. Some previous studies have indicated that satellite-derived data tends to overestimate surface Chl-*a*, compared with in situ observations and Bio-Argo data (e.g., Shang et al., 2014; Zhang et al., 2016). Vertical Chl-*a* distributions in both the model results and observations are characterized by a deep Chl-*a* maximum (DCM) at about 70 m depth, and their shapes are similar. The DCM is a ubiquitous phenomenon in upper oceans due to biological-chemical-physical interaction (Cullen, 2015). Vertical distribution of nitrate, as the primary limiting nutrient in the study area, was checked to validate the model for nutrient simulations (Figure S5 in Supporting Information S1). The result suggests that the vertical structure of model nitrate basically agrees with the observations. The above validations demonstrate that although there are some errors, the model results are credible and good enough for this study.

### 2.2. Composite Analysis

There were 226 TCs (Saffir-Simpson category ≥1) occurring in the study area from 2005 to 2022 (Figure 1). To figure out the general characteristics of 3D biogeochemical responses to the TC, a composite analysis within the study area following Wang (2020) and Wang and Xiu (2022) was conducted (Figure S6 in Supporting Information S1). The position of a TC at 12:00 a.m. in a day during its lifetime was taken as a TC location. In total, 946 TC locations were obtained from 226 TCs for the composite analysis. Within a 300 km radius from each TC location, model daily mean results during a period from 10 days before to 70 days after the TC passage were

selected. To eliminate seasonal changes in climate state, the daily anomaly results were calculated by removing the climatic mean values on the corresponding calendar date of the year from original model daily results. All anomaly results were interpolated to a standard Cartesian coordinate system with a grid interval of 5 km in horizontal direction and standard depths in vertical. In this coordinate system, $Y$ coordinate is along the TC moving track and $X$ is perpendicular to the track with positive values on its right looking in the TC moving direction. After that, the system horizontally rotates an angle so that the positive $Y$-axis points north. The TC-induced changes ($\Delta$) were defined as the differences between original anomalies and the mean anomalies during the period of 3–10 days before the TC passage (the former minus the latter).

## 3. Results and Discussion

Seen from Figures 2a and 2b, the spatial and temporal patterns of TC-induced Chl-*a* changes ($\Delta$Chl-*a*) suggest opposite responses between the surface and subsurface layers during and after the TC passage. The vertical structures of $\Delta$Chl-*a* (Figures 2c–2j) show that the obvious changes are mainly located within a 100 km radius from the TC center, with the strongest responses occurring 1 day after the TC passage. Significance testing using Student's *t*-test indicates that during and after the TC passage, the mean $\Delta$Chl-*a* values at various depths and times within the central 100 km area are significantly different from zero ($p < 0.05$) at the 95% confidence level (Table S1 in Supporting Information S1). The exception occurs at approximately 80 m depth in some days with the values negligible and statistically indistinguishable from zero.

Due to the existence of a DCM in the vertical Chl-*a* structure, TC-induced upwelling and vertical mixing cause Chl-*a* to increase (decrease) in the surface (subsurface) layer. The temporal variation of $\Delta$Chl-*a* (Figure 2 and Figure S7 in Supporting Information S1) indicates that a rapid increase appears in surface Chl-*a*, peaking one day after the TC passage with a maximum value of 0.07 mg/m$^3$. Simultaneously, the most significant reduction in Chl-*a* happens at approximately 120 m depth with a minimum $\Delta$Chl-*a* of $-0.1$ mg/m$^3$. Similar results have also been observed by BGC-*A*rgo floats in a few case studies (Chai et al., 2021; Qiu et al., 2021). Some composite results based on daily satellite data from the Moderate Resolution Imaging Spectroradiometer onboard NASA's satellite EOS-Aqua (MODIS) suggest that surface Chl-*a* peaks approximately 3 days after the TC passage (Jiang et al., 2023; Wang, 2020). However, the results obtained from the Advanced Himawari Imager onboard the Himawari-8 geostationary satellite with hyper temporal image acquisition capability show that Chl-*a* reaches its highest value on the first day after the TC passage, indicating a quicker and stronger response than that observed by MODIS (J. Y. Lin et al., 2022). This is consistent with our model results.

Although biogeochemical processes could be altered by the TC owing to changes in the vertical distribution of phytoplankton and nutrient content in the upper ocean, it takes some time for phytoplankton growth and mortality. Therefore, immediate changes in Chl-*a* in the upper ocean are almost the result of Chl-*a* redistribution during the TC period. In order to compare the effects of TC-induced dynamic processes on Chl-*a* at different depths, the vertical structures of area-averaged $\Delta$Chl-*a* within a 100 km radius from the TC center 1 day after the TC passage and the corresponding contributions of upwelling and other factors (mainly vertical mixing) are shown in Figure S8a in Supporting Information S1. The combined effects of upwelling and vertical mixing lead to the redistribution of Chl-*a*. The upwelling brings subsurface waters upward, resulting in negative $\Delta$Chl-*a* in the subsurface layer. Vertical mixing tends to make the Chl-*a* in upper layer uniform when the upwelling transports subsurface Chl-*a* to the surface layer.

Nitrate is often used as the representative nutrient in the N-limited region, just like the study region in this work, for phytoplankton growth above the light-limited layer (M. Dai et al., 2023). The area-averaged nitrate changes ($\Delta$nitrate) within a 100 km radius from the TC center 1 day after the TC passage are positive in the whole volume above 300 m depth as shown in Figure S8b in Supporting Information S1, indicating the uplift of nitrate due to the TC influence. TC-induced upwelling dominates in the nitrate increase below approximately 50 m, while TC-induced vertical mixing is the primary factor above. The greatest significant increase occurs in the layer between 100 and 200 m depth (Figure S8b and Table S2 in Supporting Information S1), with a maximum value of 1.0 mmol/m$^3$. It is owing to strong upwelling and pronounced vertical gradient of nitrate in this layer (Figures S8b and S8d in Supporting Information S1).

After the TC passage, the TC-induced physical processes gradually decay, and the subsequent biological processes become the dominant factors influencing the variation of $\Delta$Chl-*a* in the upper ocean. Figure 3 shows the temporal evolutions of $\Delta$Chl-*a* and $\Delta$nitrate along the cross-track axis. Note that the signals of near-inertial

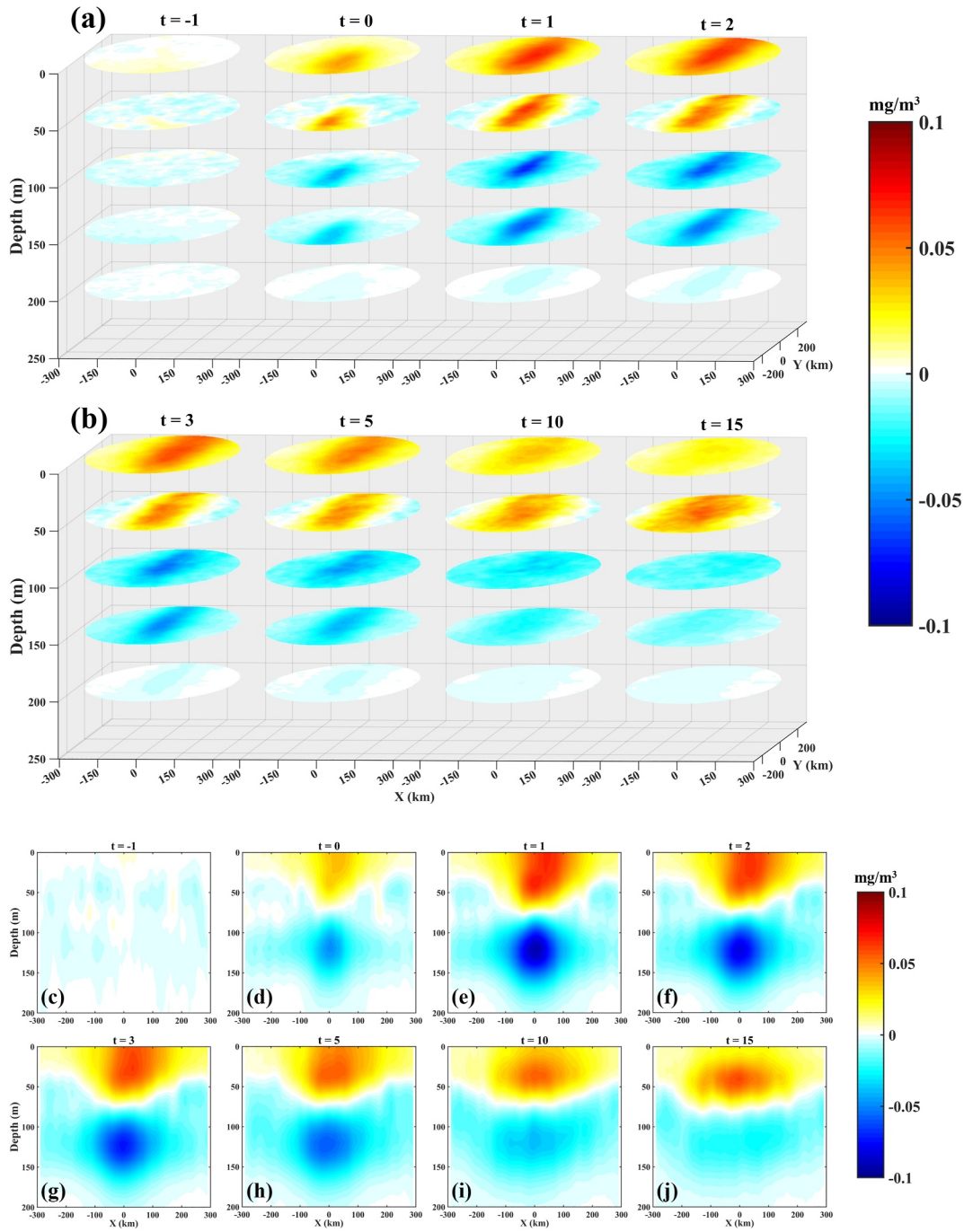


**Figure 2.** Temporal variations of (a, b) horizontal distributions of ΔChl-*a* at 0, 50, 100, 150 m depth and (c–j) vertical structure of ΔChl-*a* in the cross-track transect ($Y = 0$). The positive (negative) value on the *X*-axis is the distance to the right (left) of the tropical cyclone (TC) track, and the positive (negative) value on the *Y*-axis is the distance ahead (rear) of the TC center, facing in the moving direction of TC. The days before (after) TC passage is denoted as the negative (positive) value of *t*, and $t = 0$ indicates the day of the TC passage.

internal waves are absent since daily averaged model outputs are adopted. At the sea surface, Chl-*a* obviously increases after the TC passage, especially on the right side of the TC track. Subsequently, the increase of Chl-*a* rapidly attenuates because the augments of nitrate are limited for phytoplankton growth. This is similar to the findings from satellite data (Jiang et al., 2023; J. Y. Lin et al., 2022; Wang, 2020). At 50 m depth, TC-induced physical processes lead to marked rises in Chl-*a* and nitrate (Figure S8 in Supporting Information S1). The

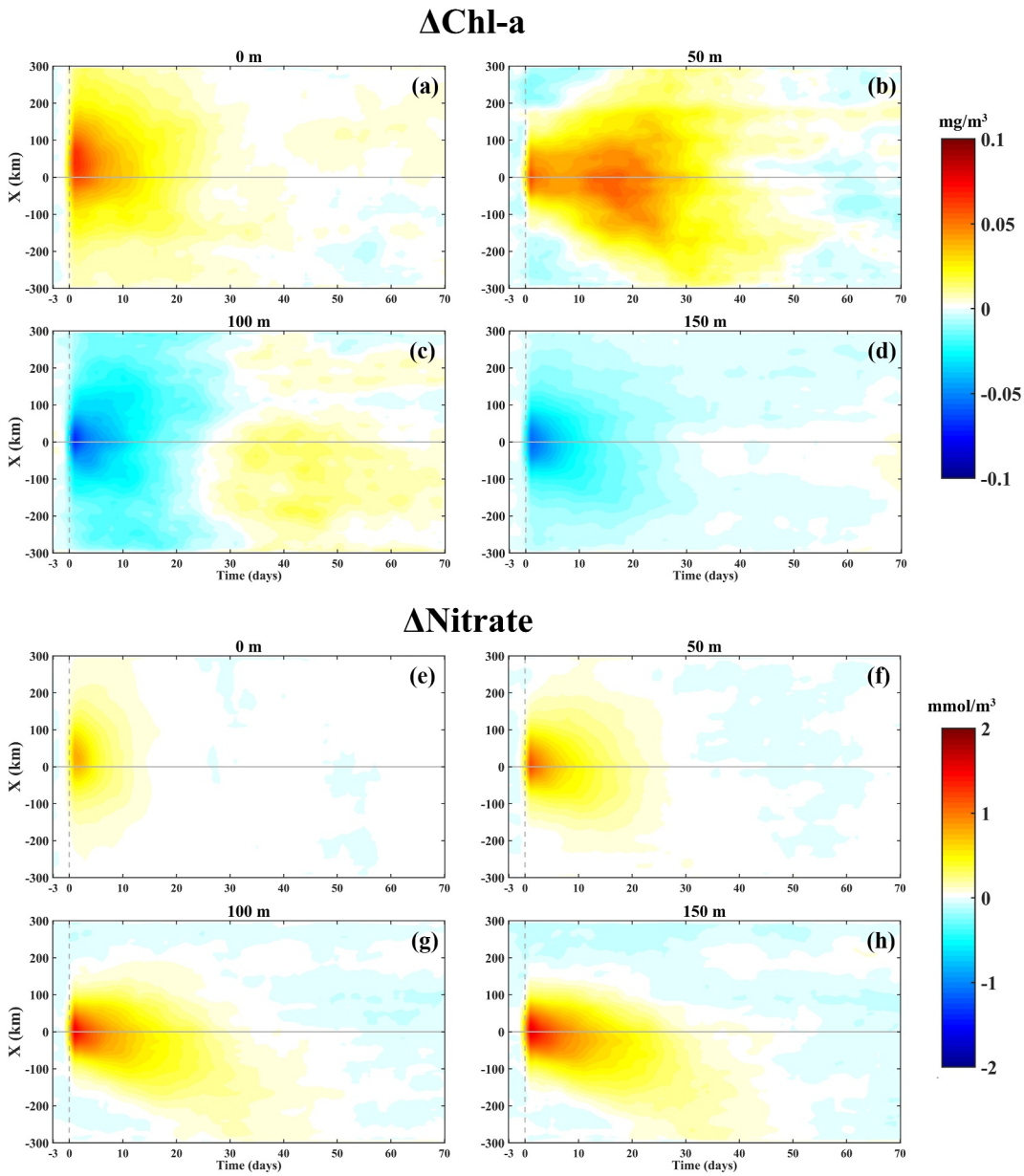


**Figure 3.** Temporal evolutions of (a–d) ΔChl-*a* and (e–h) Δnitrate along the cross-track axis ($Y = 0$) at the 0, 50, 100, 150 m depth. The gray dashed and solid lines in each panel denote the day of the tropical cyclone (TC) passage and the position of the TC center, respectively.

increased nitrate facilitates phytoplankton growth. Consequently, Chl-*a* further increases after the TC passage (Figure 3b and Figure S7 in Supporting Information S1), with high ΔChl-*a* lasting for more than 30 days. In the subsurface layer near the DCM depth (around 100 m), although nitrate is increased markedly after the TC passage, Chl-*a* drops sharply at first and then this reduction gradually disappears, and 3 weeks later the Chl-*a* has a slight increase. In the lower euphotic layer around 150 m depth, there is a similar drop in Chl-*a*, but no slight increase 3 weeks later. This layer was light-limited for phytoplankton growth attributed to weak illumination (Dai et al., 2023).

The above results indicate that Chl-*a* responses to the TC are notably different at different depths. Due to the distinct vertical distributions of Chl-*a* and nitrate, TC-induced physical processes cause varying ΔChl-*a* and Δnitrate at different depths, leading to diverse changes in phytoplankton growth and mortality rates. Thus, TC-induced vertical redistributions of Chl-*a* and nutrients, along with simultaneous changes in biological processes,

jointly determine the temporal evolution of ΔChl-*a* in the upper ocean. In particular, the favorable conditions created by the TC sustain high ΔChl-*a* around the 50 m depth, just below the MLD of about 30 m, for a long time. Similar phenomena have also been captured by observations. Yu et al. (2022) conducted a cruise about 1 week after the passage of TC Talim across the East China Sea in September 2017, indicating that the most significant increase in Chl-*a* happened under the mixed layer in the TC affected area, compared to the surrounding unaffected waters. Based on BGC-Argo float profiles, Zheng and Zhang (2023) found that TC Hagibis redistributed Chl-*a* vertically (increasing surface layer Chl-*a* above approximately 50 m depth and decreasing subsurface Chl-*a* below 50 m) at first, and nearly 1 week after the TC passage, surface Chl-*a* decreased close to pre-TC status while the Chl-*a* around the 40 m depth remained high values.

It is noteworthy that, as Δnitrate restores, the high nitrate anomalies gradually shift toward the left side of the TC track in the subsurface layer (Figure 3). In addition, the subsurface cooling exhibits a similar feature (Figure S9 in Supporting Information S1). These suggest that this phenomenon is driven by physical processes rather than biological processes. This feature primarily occurs in the subsurface layer and is not evident in the surface layer (Figure S10 in Supporting Information S1). In the surface layer, the cooling is basically concentrated in the TC central area with its core slightly to the right (Figure S9a in Supporting Information S1), and the high nitrate anomalies rapidly diminish due to biological utilization (Figure 3e). The composite results of the temperature response to TCs obtained from Argo data also show that there is a similar leftward movement of temperature anomaly in the subsurface layer, but no such movement in the surface layer (S. Lin et al., 2017).

The leftward-shifting features of both nitrate and temperature anomalies in the subsurface are related to the advection effect of horizontal currents. Although significant changes in the currents are caused by the TC, they gradually return to the background state soon after the TC passage. Comparison of the background currents between surface and subsurface layers (Figure S9 in Supporting Information S1), there is a component of currents toward the left side of the TC track. Given that the direction of surface currents before the TC is generally aligned with the moving direction of the TC, subsurface currents deflect toward the left of the TC's moving direction, leading to the leftward shift of nitrate and temperature anomalies in the subsurface layer. The distribution of density $\sigma$ along the meridional section at 135°E (Figure S11a in Supporting Information S1) indicates that the density within the upper 200 m generally increases with latitude in the north of 15°N. The 135°E meridional section is selected as the representation because the average position of the TC centers in our study is approximately at 135°E, 20°N, and in this area the meridional gradient of density is much larger than the zonal gradient. This density distribution generates a westward baroclinic geostrophic flow according to the geostrophic balance. TC-induced currents weaken significantly with increasing depth, especially in the left of the TC track (Figure S9 in Supporting Information S1). Ultimately, the subsurface currents point to the left and back of the TC moving track which is in the northwest direction (Figure S11b in Supporting Information S1). Consequently, in the subsurface layer, TC-induced nitrate and temperature anomalies gradually shift to the left side of the TC track.

To figure out the net impacts of the TC on the total biomass in the upper ocean, the Chl-*a* above 200 m depth is integrated vertically (Chl-$a_{200}$), and the temporal evolution of Chl-$a_{200}$ changes (ΔChl-$a_{200}$) across the TC track is obtained (Figure 4a). The results show an obvious decrease in Chl-$a_{200}$ shortly after the TC passage with a minimum ΔChl-$a_{200}$ of −2.3 mg/m$^2$, especially on the left side of the TC track owing to the rightward bias of nutrient increase in the surface layer. Although a lot of nutrients are uplifted into the euphotic layer, reduced illumination and lowered water temperature just after the TC passage inhibit phytoplankton growth. Additionally, after the TC-induced vertical Chl-*a* redistribution mentioned previously, the high Chl-*a* anomalies in the surface layer decrease quickly due to the death of much phytoplankton, and phytoplankton growth in the subsurface layer is limited by weak illumination (Figure 3 and Figure S7 in Supporting Information S1). These are responsible for the decrease of Chl-$a_{200}$ after the TC passage. Subsequently, as the temperature and sunlight recovering over time, the phytoplankton growth rate in the upper ocean increases, becoming quite higher than before the TC passage due to the increased nutrient content. Consequently, ΔChl-$a_{200}$ gradually shifts from negative to positive with a maximum value of 2.0 mg/m$^2$. Furthermore, the ΔChl-$a_{200}$ on the left side of the TC track is slightly higher than that on the right side during this period since nutrient-rich water tends to be advected toward the left side of the TC track (Figure 3). With the extra nutrients (positive Δnitrate) are depleted, ΔChl-$a_{200}$ begins to decrease. The evolution of ΔChl-$a_{200}$ integrated over composite area (ΔChl-$a_{total}$) indicates that the total biomass within the TC affected area reaches its minimum (−0.21 Gg, 1Gg = $10^9$g) 4 days after the TC passage and its maximum (0.28 Gg) about 30 days later. Subsequently, the total biomass restores to pre-TC status after approximately 1 month (Figure 4b). Similar results were observed by a BGC-Argo float (ID: 2902750) when TC Trami, a

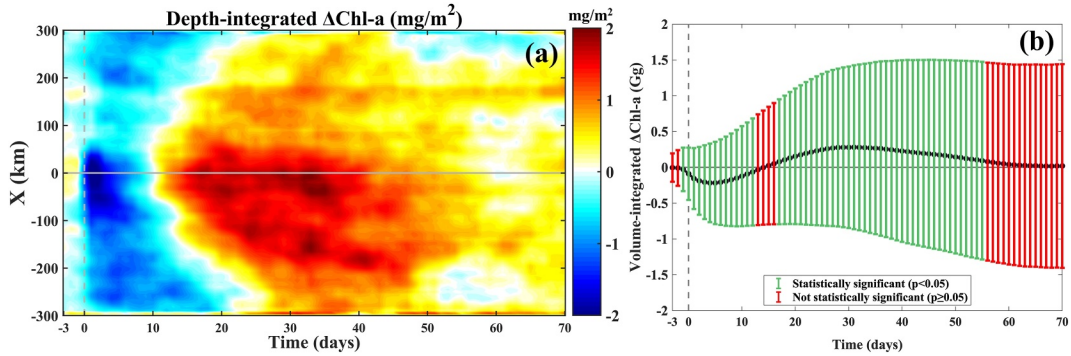


**Figure 4.** (a) Temporal evolution of depth-integrated ΔChl-*a* above 200 m depth along the cross-track axis. (b) Time series of volume-integrated ΔChl-*a* above 200 m depth. The vertical error bars in (b) show one standard deviation above and below the corresponding ΔChl-*a* values. Green error bars denote statistically significant results (significantly different from zero), and red bars indicate non-significant ones (statistically indistinguishable from zero).

category 5 TC, affected the sea area south of Japan, Northwest Pacific in September and October 2018 (Figure S12a in Supporting Information S1). During the period from September 18 to October 24, the BGC-Argo recorded Chl-*a* profiles with the 1-day interval in the TC influence sea area. The time series of Chl-$a_{200}$ calculated from these Chl-*a* profiles demonstrated that compared with the pre-TC average value (20.3 mg/m$^2$), the average Chl-$a_{200}$ within 11 days (day 1–11) after the TC passage decreased by about 1.5 mg/m$^2$, and then the average from day 12 to day 23 rose significantly with a net increase of 2.4 mg/m$^2$ (Figure S12b in Supporting Information S1). These results indicate that the TC could promote the net growth of phytoplankton, potentially enhancing biological carbon sequestration.

## 4. Conclusions

In this study, we present the first 3D analysis of biogeochemical responses to TCs in the Northwest Pacific, employing a composite method based on coupled physical-biogeochemical model simulations. Our 3D composite results reveal that area-averaged ΔChl-*a* within a 100 km radius from the TC track exhibits a depth-dependent temporal evolution due to the combined effect of physical processes (upwelling and vertical mixing) and biological processes (phytoplankton growth and mortality). Surface ΔChl-*a* increases rapidly due to vertical mixing-driven Chl-*a* redistribution, but declines after ∼1 day as nutrient depletion enhances phytoplankton mortality. In the 50 m layer, a rapid ΔChl-*a* increase occurs through upwelling-induced redistribution and subsequent phytoplankton growth, peaking at ∼20 days. In the 100 m layer, ΔChl-*a* initially decreases due to the redistribution by both upwelling and vertical mixing, then gradually increases with nutrient-enhanced phytoplankton growth, becoming positive after ∼30 days. Following an initial rapid decrease, ΔChl-*a* in the 150 m layer slowly recovers to pre-TC levels. The evolution of integrated ΔChl-*a* above 200 m indicates that total biomass within the TC affected area reaches a minimum 4 days after the TC passage and peaks at about 30 days later, then gradually restores to pre-TC levels by ∼60 days. This progression yields a net biomass increase attributable to TC forcing, suggesting that TCs may enhance ocean primary production and strengthen carbon sequestration capacity. Additionally, we found that in the Northwest Pacific, the westward geostrophic advection–driven by meridional density gradients–generates larger subsurface nutrient and Chl-*a* positive anomalies in the left of the generally northwestward TC track than those in the right.

Although our model captures essential characteristics of upper-ocean biogeochemical responses to TCs, the simulations cannot fully replicate actual ocean conditions. Further work requires additional observational data to validate the 3D composite results derived from model simulations.

## Data Availability Statement

The track data of TCs were taken from the IBTrACS data set via Gahtan et al. (2024). SST and SSS data were obtained from Remote Sensing System (2022) and Meissner et al. (2024), respectively. Surface Chl-*a* data were

from MODIS (NASA Ocean Biology Processing Group, 2014). Profiles of Argo floats are available via Argo Program (Argo, 2000).

**Acknowledgments**
This work was jointly supported by the State Key R&D project (2022YFF0801404), Xiamen University President's Fund (20720240020), and the National Natural Science Foundation of China (41776015).

## References

Argo. (2000). Argo float data and metadata from Global Data Assembly Centre (Argo GDAC). [Dataset]. *SEANOE*. https://doi.org/10.17882/42182

Babin, S. M., Carton, J. A., Dickey, T. D., & Wiggert, J. D. (2004). Satellite evidence of hurricane-induced phytoplankton blooms in an oceanic desert. *Journal of Geophysical Research*, *109*(C3), C03043. https://doi.org/10.1029/2003jc001938

Chacko, N. (2017). Chlorophyll bloom in response to tropical cyclone Hudhud in the Bay of Bengal: Bio-argo subsurface observations. *Deep Sea Research Part I: Oceanographic Research Papers*, *124*, 66–72. https://doi.org/10.1016/j.dsr.2017.04.010

Chai, F., Dugdale, R. C., Peng, T.-H., Wilkerson, F. P., & Barber, R. T. (2002). One-dimensional ecosystem model of the equatorial Pacific upwelling system. Part I: Model development and silicon and nitrogen cycle. *Deep-Sea Research II*, *49*(13–14), 2713–2745. https://doi.org/10.1016/S0967-0645(02)00055-3

Chai, F., Johnson, K. S., Claustre, H., Xing, X., Wang, Y., Boss, E., et al. (2020). Monitoring ocean biogeochemistry with autonomous platforms. *Nature Reviews Earth & Environment*, *1*(6), 315–326. https://doi.org/10.1038/s43017-020-0053-y

Chai, F., Wang, Y., Xing, X., Yan, Y., Xue, H., Wells, M., & Boss, E. (2021). A limited effect of sub-tropical typhoons on phytoplankton dynamics. *Biogeosciences*, *18*(3), 849–859. https://doi.org/10.5194/bg-2020-310

Cossarini, G., Mariotti, L., Feudale, L., Mignot, A., Salon, S., Taillandier, V., et al. (2019). Towards operational 3D-var assimilation of chlorophyll biogeochemical-argo float data into a biogeochemical model of the Mediterranean Sea. *Ocean Modelling*, *133*, 112–128. https://doi.org/10.1016/j.ocemod.2018.11.005

Cullen, J. J. (2015). Subsurface chlorophyll maximum layers: Enduring enigma or mystery solved? *Annual Review of Marine Science*, *7*(1), 207–239. https://doi.org/10.1146/annurev-marine-010213-135111

Dai, A. (2017). Dai and Trenberth global river flow and continental discharge dataset. [Dataset]. *Research Data Archive at the National Center for Atmospheric Research*. https://doi.org/10.5065/D6V69H1T

Dai, M., Luo, Y. W., Achterberg, E. P., Browning, T. J., Cai, Y., Cao, Z., et al. (2023). Upper ocean biogeochemistry of the oligotrophic North Pacific Subtropical Gyre: From nutrient sources to carbon export. *Reviews of Geophysics*, *61*(3), e2022RG000800. https://doi.org/10.1029/2022rg000800

Dickey, T., Frye, D., McNeil, J., Manov, D., Nelson, N., Sigurdson, D., et al. (1998). Upper-ocean temperature response to Hurricane Felix as measured by the Bermuda testbed mooring. *Monthly Weather Review*, *126*(5), 1195–1201. https://doi.org/10.1175/1520-0493(1998)126<1195:uotrth>2.0.co;2

Dickey, T. D., & Simpson, J. J. (1983). The sensitivity of the upper ocean structure to time varying wind direction. *Geophysical Research Letters*, *10*(2), 133–136. https://doi.org/10.1029/GL010i002p00133

Egbert, G. D., & Erofeeva, S. Y. (2002). Efficient inverse modeling of barotropic ocean tides. *Journal of Atmospheric and Oceanic Technology*, *19*(2), 183–204. https://doi.org/10.1175/1520-0426(2002)019<0183:eimobo>2.0.co;2

Foltz, G. R., Balaguru, K., & Leung, L. R. (2015). A reassessment of the integrated impact of tropical cyclones on surface chlorophyll in the western subtropical North Atlantic. *Geophysical Research Letters*, *42*(4), 1158–1164. https://doi.org/10.1002/2015gl063222

Gahtan, J., Knapp, K. R., Schreck, C. J., Diamond, H. J., Kossin, J. P., & Kruk, M. C. (2024). International Best Track Archive for Climate Stewardship (IBTrACS) project, version 4r01 [Dataset]. *NOAA National Centers for Environmental Information*. https://doi.org/10.25921/82ty-9e16

Garcia, H. E., Boyer, T. P., Baranova, O. K., Locarnini, R. A., Mishonov, A. V., Grodsky, A., et al. (2019). World Ocean Atlas 2018 [Dataset]. *NOAA National Centers for Environmental Information*. https://doi.org/10.25923/tzyw-rp36

Gierach, M. M., & Subrahmanyam, B. (2008). Biophysical responses of the upper ocean to major Gulf of Mexico hurricanes in 2005. *Journal of Geophysical Research*, *113*(C4), C04029. https://doi.org/10.1029/2007jc004419

Hanshaw, M. N., Lozier, M. S., & Palter, J. B. (2008). Integrated impact of tropical cyclones on sea surface chlorophyll in the North Atlantic. *Geophysical Research Letters*, *35*(1), L01601. https://doi.org/10.1029/2007gl031862

Hersbach, H., Bell, B., Berrisford, P., Biavati, G., Horányi, A., Muñoz Sabater, J., et al. (2023). ERA5 hourly data on single levels from 1940 to present [Dataset]. *Copernicus Climate Change Service (C3S) Climate Data Store (CDS)*. https://doi.org/10.24381/cds.adbb2d47

Jiang, Y., Wang, Y., Tian, X., Lin, S., Chen, S., Yu, J., & Chai, F. (2023). Upper ocean structure determines the contrasting typhoon-induced chlorophyll-a responses in the northwest Pacific. *Geophysical Research Letters*, *50*(10), e2023GL102930. https://doi.org/10.1029/2023gl102930

Kao, K. J., Huang, W. J., Chou, W. C., Gong, G. C., & Weerathunga, V. (2023). Factors controlling the sea surface partial pressure of carbon dioxide in upwelling regions: A case study of the southern East China Sea before and after Typhoon Maria. *Journal of Geophysical Research: Oceans*, *128*(2), e2022JC019195. https://doi.org/10.1029/2022jc019195

Kossin, J. P., Olander, T. L., & Knapp, K. R. (2013). Trend analysis with a new global record of tropical cyclone intensity. *Journal of Climate*, *26*(24), 9960–9976. https://doi.org/10.1175/jcli-d-13-00262.1

Lellouche, J. M., Greiner, E., Le Galloudec, O., Garric, G., Regnier, C., Drevillon, M., et al. (2018). Recent updates to the copernicus marine service global ocean monitoring and forecasting real-time 1/12° high-resolution system. *Ocean Science*, *14*(5), 1093–1126. https://doi.org/10.5194/os-14-1093-2018

Li, J., Yang, Y., Wang, G., Cheng, H., & Sun, L. (2021). Enhanced oceanic environmental responses and feedbacks to super Typhoon Nida (2009) during the sudden-turning stage. *Remote Sensing*, *13*(14), 2648. https://doi.org/10.3390/rs13142648

Li, Y., Yang, D., Xu, L., Gao, G., He, Z., Cui, X., et al. (2022). Three types of typhoon-induced upwellings enhance coastal algal blooms: A case study. *Journal of Geophysical Research: Oceans*, *127*(5), e2022JC018448. https://doi.org/10.1029/2022jc018448

Lin, I., Liu, W. T., Wu, C.-C., Wong, G. T. F., Hu, C., Chen, Z., et al. (2003). New evidence for enhanced ocean primary production triggered by tropical cyclone. *Geophysical Research Letters*, *30*(13), 1718. https://doi.org/10.1029/2003gl017141

Lin, I.-I. (2012). Typhoon-induced phytoplankton blooms and primary productivity increase in the western North Pacific subtropical ocean. *Journal of Geophysical Research*, *117*(C3), C03039. https://doi.org/10.1029/2011jc007626

Lin, J.-Y., Ho, H., & Zheng, Z.-W. (2022). Improved understanding of typhoon-induced immediate chlorophyll-a response using Advanced Himawari Imager (AHI) onboard Himawari-8. *Remote Sensing*, *14*(23), 6055. https://doi.org/10.3390/rs14236055

Lin, S., Zhang, W.-Z., Shang, S.-P., & Hong, H.-S. (2017). Ocean response to typhoons in the western North Pacific: Composite results from argo data. *Deep Sea Research Part I: Oceanographic Research Papers*, *123*, 62–74. https://doi.org/10.1016/j.dsr.2017.03.007

Mei, W., Lien, C.-C., Lin, I. I., & Xie, S.-P. (2015). Tropical cyclone–induced ocean response: A comparative study of the South China Sea and tropical northwest Pacific. *Journal of Climate*, *28*(15), 5952–5968. https://doi.org/10.1175/jcli-d-14-00651.1

Meissner, T., Wentz, F. J., Manaster, A., Lindsley, R., Brewer, M., & Densberger, M. (2024). Remote sensing systems SMAP ocean surface salinities, version 6.0 validated release [Dataset]. *Remote Sensing Systems*. https://doi.org/10.5067/SMP60-3SPCS

Naik, H., Naqvi, S. W. A., Suresh, T., & Narvekar, P. V. (2008). Impact of a tropical cyclone on biogeochemistry of the central Arabian Sea. *Global Biogeochemical Cycles*, *22*(3), GB3020. https://doi.org/10.1029/2007gb003028

NASA Ocean Biology Processing Group. (2014). Moderate Resolution Imaging Spectroradiometer (MODIS) level-3 ocean color data, version R2014.0.2 [Dataset]. *NASA Ocean Biology Distributed Active Archive Center*. https://doi.org/10.5067/JCQB8QALDOYD

Pan, G., Chai, F., Tang, D., & Wang, D. (2017). Marine phytoplankton biomass responses to typhoon events in the South China Sea based on physical-biogeochemical model. *Ecological Modelling*, *356*, 38–47. https://doi.org/10.1016/j.ecolmodel.2017.04.013

Price, J. F. (1981). Upper ocean response to a hurricane. *Journal of Physical Oceanography*, *11*(2), 153–175. https://doi.org/10.1175/1520-0485(1981)011<0153:uortah>2.0.co;2

Price, J. F., Sanford, T. B., & Forristall, G. Z. (1994). Forced stage response to a moving hurricane. *Journal of Physical Oceanography*, *24*(2), 233–260. https://doi.org/10.1175/1520-0485(1994)024<0233:fsrtam>2.0.co;2

Qiu, G., Xing, X., Chai, F., Yan, X.-H., Liu, Z., & Wang, H. (2021). Far-field impacts of a super typhoon on upper ocean phytoplankton dynamics. *Frontiers in Marine Science*, *8*, 643608. https://doi.org/10.3389/fmars.2021.643608

Remote Sensing Systems. (2022). MW-IR optimum interpolated SST data set. Ver. 5.1 [Dataset]. *PO.DAAC, CA, USA*. https://doi.org/10.5067/GHMWI-4FR51

Russell, P., & Horvat, C. (2023). Extreme South Pacific phytoplankton blooms induced by tropical cyclones. *Geophysical Research Letters*, *50*(5), e2022GL100821. https://doi.org/10.1029/2022gl100821

Shang, S. L., Dong, Q., Hu, C., Lin, G., Li, Y. H., & Shang, S. P. (2014). On the consistency of MODIS chlorophyll a products in the northern South China Sea. *Biogeosciences*, *11*(2), 269–280. https://doi.org/10.5194/bg-11-269-2014

Shchepetkin, A. F., & McWilliams, J. C. (2005). The regional oceanic modeling system (ROMS): A split-explicit, free-surface, topography-following-coordinate oceanic model. *Ocean Modelling*, *9*(4), 347–404. https://doi.org/10.1016/j.ocemod.2004.08.002

Siswanto, E., Morimoto, A., & Kojima, S. (2009). Enhancement of phytoplankton primary productivity in the southern East China Sea following episodic typhoon passage. *Geophysical Research Letters*, *36*(11), L11603. https://doi.org/10.1029/2009gl037883

Subrahmanyam, B., Rao, K. H., Srinivasa Rao, N., Murty, V. S. N., & Sharp, R. J. (2002). Influence of a tropical cyclone on chlorophyll-a concentration in the Arabian Sea. *Geophysical Research Letters*, *29*(22), 1–4. https://doi.org/10.1029/2002gl015892

Sun, J., Oey, L.-Y., Chang, R., Xu, F., & Huang, S.-M. (2015). Ocean response to Typhoon Nuri (2008) in western Pacific and South China Sea. *Ocean Dynamics*, *65*(5), 735–749. https://doi.org/10.1007/s10236-015-0823-0

Sun, L., Yang, Y.-J., Xian, T., Lu, Z.-M., & Fu, Y.-F. (2010). Strong enhancement of chlorophyll a concentration by a weak typhoon. *Marine Ecology Progress Series*, *404*, 39–50. https://doi.org/10.3354/meps08477

Wang, T., Chai, F., Xing, X., Ning, J., Jiang, W., & Riser, S. C. (2021). Influence of multi-scale dynamics on the vertical nitrate distribution around the Kuroshio extension: An investigation based on BGC-argo and satellite data. *Progress in Oceanography*, *193*, 102543. https://doi.org/10.1016/j.pocean.2021.102543

Wang, Y. (2020). Composite of typhoon-induced sea surface temperature and chlorophyll-a responses in the South China Sea. *Journal of Geophysical Research: Oceans*, *125*(10), e2020JC016243. https://doi.org/10.1029/2020jc016243

Wang, Y., & Xiu, P. (2022). Typhoon footprints on ocean surface temperature and chlorophyll-a in the South China Sea. *Science of the Total Environment*, *840*, 156686. https://doi.org/10.1016/j.scitotenv.2022.156686

Wang, Z., Bovik, A. C., Sheikh, H. R., & Simoncelli, E. P. (2004). Image quality assessment: From error visibility to structural similarity. *IEEE Transactions on Image Processing*, *13*(4), 600–612. https://doi.org/10.1109/tip.2003.819861

Webster, P. J., Holland, G. J., Curry, J. A., & Chang, H. R. (2005). Changes in tropical cyclone number, duration, and intensity in a warming environment. *Science*, *309*(5742), 1844–1846. https://doi.org/10.1126/science.1116448

Xiu, P., & Chai, F. (2012). Spatial and temporal variability in phytoplankton carbon, chlorophyll, and nitrogen in the North Pacific. *Journal of Geophysical Research*, *117*(C11). https://doi.org/10.1029/2012jc008067

Xiu, P., Chai, F., Shi, L., Xue, H., & Chao, Y. (2010). A census of eddy activities in the South China Sea during 1993–2007. *Journal of Geophysical Research*, *115*(C03012). https://doi.org/10.1029/2009jc005657

Ye, H. J., Sui, Y., Tang, D. L., & Afanasyev, Y. D. (2013). A subsurface chlorophyll a bloom induced by typhoon in the South China Sea. *Journal of Marine Systems*, *128*, 138–145. https://doi.org/10.1016/j.jmarsys.2013.04.010

Yu, P., Yang, X., Wang, B., Li, T., Tao, B., Zheng, M., & Bai, Y. (2022). Moderate $CO_2$ sink due to phytoplankton bloom following a typhoon passage over the East China Sea. *Continental Shelf Research*, *238*, 104696. https://doi.org/10.1016/j.csr.2022.104696

Zhang, W.-Z., Wang, H., Chai, F., & Qiu, G. (2016). Physical drivers of chlorophyll variability in the open South China Sea. *Journal of Geophysical Research: Oceans*, *121*(9), 7123–7140. https://doi.org/10.1002/2016JC011983

Zhao, H., Tang, D., & Wang, Y. (2008). Comparison of phytoplankton blooms triggered by two typhoons with different intensities and translation speeds in the South China Sea. *Marine Ecology Progress Series*, *365*, 57–65. https://doi.org/10.3354/meps07488

Zhao, H., & Wang, Y. (2018). Phytoplankton increases induced by tropical cyclones in the South China Sea during 1998-2015. *Journal of Geophysical Research: Oceans*, *123*(4), 2903–2920. https://doi.org/10.1002/2017jc013549

Zheng, H., & Zhang, W.-Z. (2023). An extraordinary chlorophyll-a enhancement event jointly induced by two sequential tropical cyclones in the Kuroshio region south of Japan. *Frontiers in Marine Science*, *10*(10), 1269310. https://doi.org/10.3389/fmars.2023.1269310

Zhou, F., Chai, F., Huang, D., Xue, H., Chen, J., Xiu, P., et al. (2017). Investigation of hypoxia off the Changjiang estuary using a coupled model of ROMS-CoSiNE. *Progress in Oceanography*, *159*, 237–254. https://doi.org/10.1016/j.pocean.2017.10.008

Supporting Information for

# Composite of three-dimensional biogeochemical responses to tropical cyclones in the Northwest Pacific

Hui Zheng[1,2,3,4], Wen-Zhou Zhang[1,2,3,4*], Zhiguo Mei[1,2,3,4]

[1]College of Ocean and Earth Sciences, Fujian Provincial Key Laboratory for Coastal Ecology and Environmental Studies, Xiamen University, Xiamen, China

[2]State Key Laboratory of Marine Environmental Science, Xiamen University, Xiamen, China

[3]Coastal and Ocean Management Institute (COMI), Xiamen University, Xiamen, China

[4]Key Laboratory of Underwater Acoustic Communication and Marine Information Technology (Xiamen University), Ministry of Education, Xiamen 361102, China

## Introduction

This supporting information includes 12 figures and 2 tables to supplement the main text of the manuscript.

Figures S1: Locations of in-situ observation profiles for model validation.

Figures S2-S5: Results of model validation.

Figures S6: Schematic diagram of composite analysis.

Figures S7-S8: Vertical characteristics of biogeochemical responses to the TCs.

Tables S1-S2: Significance testing for ΔChl-a and Δnitrate.

Figures S9-S10: The shifts of temperature and nitrate anomalies toward the left side of the TC track in the subsurface layer, and the differences of currents between sea surface and corresponding depths.

Figure S11: Spatial features of climatological mean σ in the Northwest Pacific.

Figure S12: Responses of depth-integrated Chl-a to TC Trami observed by BGC-Argo 2902750.

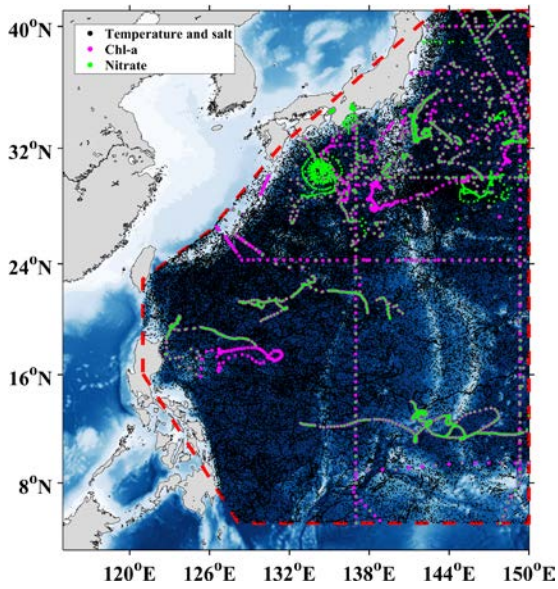


Figure S1. Locations of in-situ observation profiles for model validation. Black dots denote positions of temperature and salt profiles. Magenta and green dots denote positions of chlorophyll *a* and nitrate profiles, respectively. The area surrounded by red dashed lines delineates the study area.

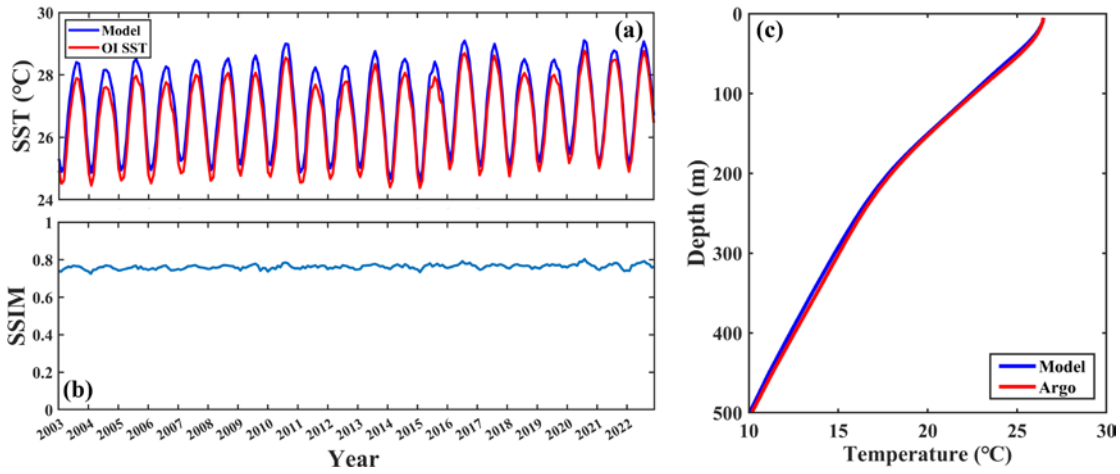


Figure S2. The validation of model temperature results. (a) Time series of monthly model SST (blue line) and the OI SST (red line). (b) Time series of SSIM between monthly model SST and the OI SST. (c) Vertical structures of temperature from model outputs (blue line) and Argo floats (red line).

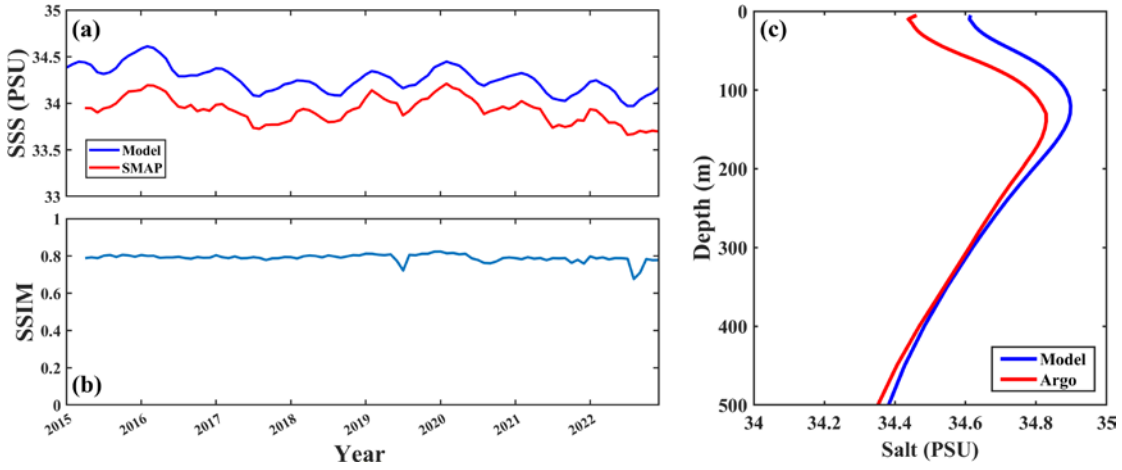


Figure S3. The validation of model salinity results. (a) Time series of monthly model SSS (blue line) and the SMAP (red line). (b) Time series of SSIM between monthly model SSS and the SMAP. (c) Vertical structures of salinity from model outputs (blue line) and Argo floats (red line).

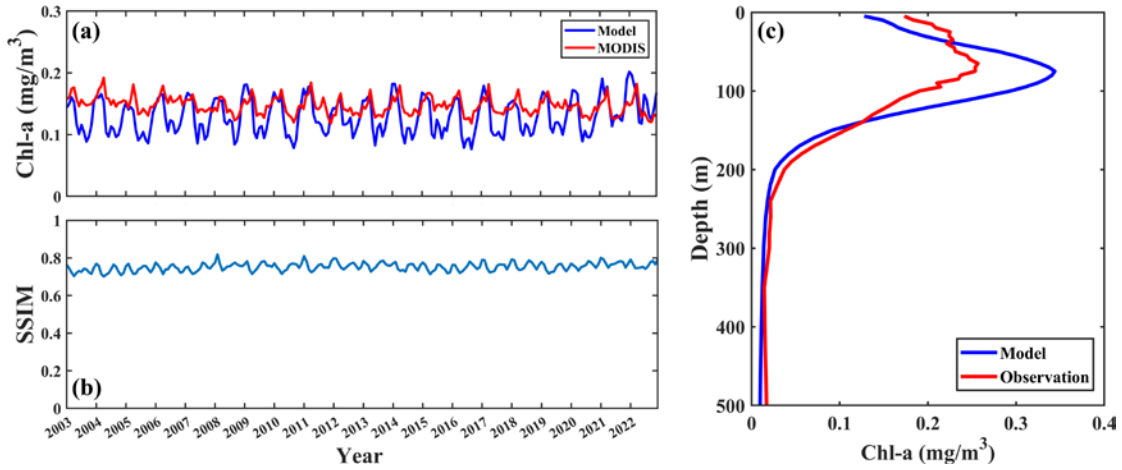


Figure S4. The validation of model Chl-a results. (a) Time series of monthly model surface Chl-a (blue line) and the MODIS (red line). (b) Time series of SSIM between monthly model surface Chl-a and the MODIS. (c) Vertical structures of Chl-a from model outputs (blue line) and observations (red line).

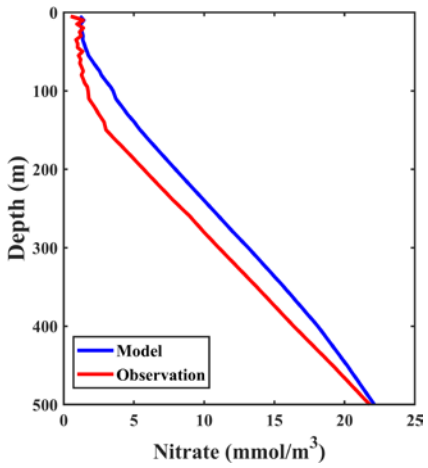


Figure S5. Vertical structures of nitrate from model outputs (blue line) and observations (red line).

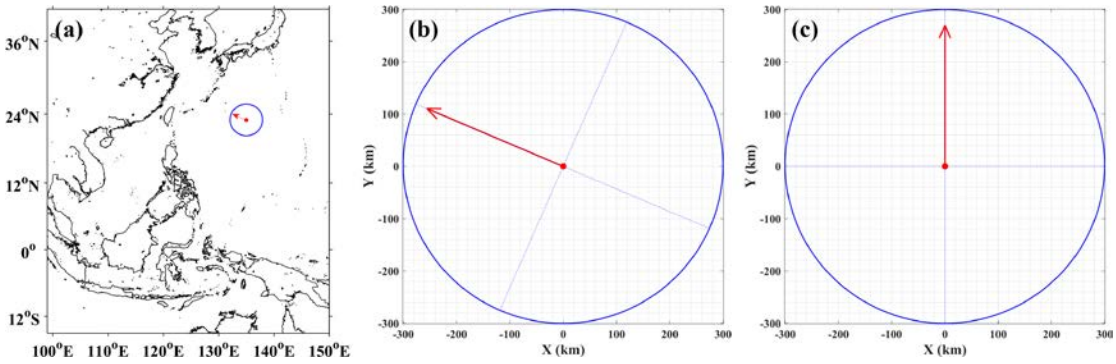


Figure S6. Schematic diagram of composite analysis. Red dots and arrows represent the center and moving direction of the TC, respectively. Blue circle denotes the distance of 300 km to the TC center.

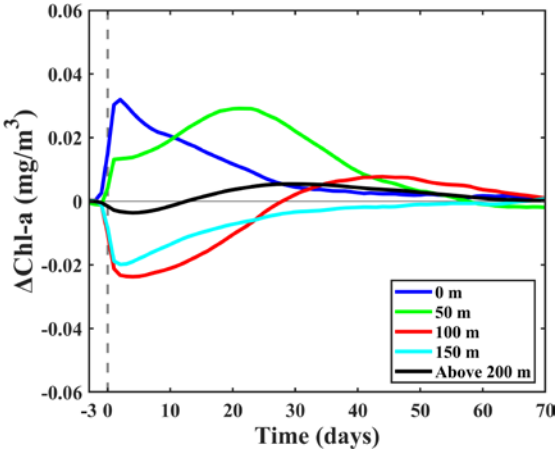


Figure S7. Time series of the area-averaged ΔChl-a at 0 (blue line), 50 (green line), 100 (red line), 150 m (cyan line) depth and mean ΔChl-a above 200 m depth (black line). The gray dashed line denotes the day of TC passage.

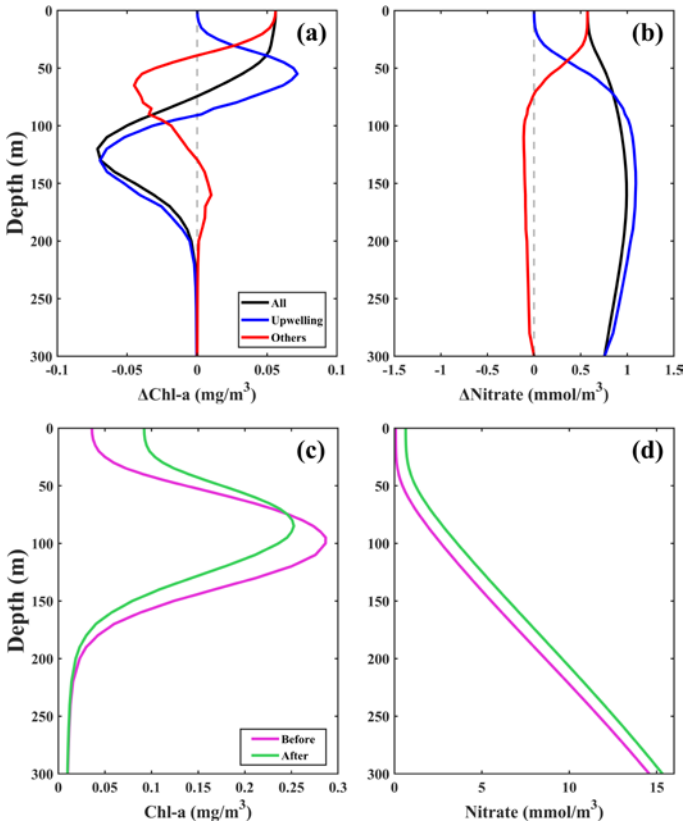


Figure S8. Vertical structures (black lines) of area-averaged (a) ΔChl-a and (b) Δnitrate within a radius of 100 km from the TC center 1 day after the TC passage. Blue and red lines represent the contributions of upwelling and other factors, respectively. Comparison of vertical structures of (c) Chl-a and (d) nitrate before the TC passage (pink lines) and 1 day after the TC passage (green lines).

Table S1. Significance testing for ΔChl-a. (T means statistically significant, and F means statistically non-significant)

| Depth (m) \ Time (Day) | t=-1 | t=0 | t=1 | t=2 | t=3 | t=5 | t=10 | t=15 |
|---|---|---|---|---|---|---|---|---|
| 0 | T | T | T | T | T | T | T | T |
| 10 | F | T | T | T | T | T | T | T |
| 20 | F | T | T | T | T | T | T | T |
| 30 | F | T | T | T | T | T | T | T |
| 40 | F | T | T | T | T | T | T | T |
| 50 | F | T | T | T | T | T | T | T |
| 60 | F | T | T | T | T | T | T | T |
| 70 | F | F | T | T | T | T | T | T |
| 80 | F | F | F | T | T | T | F | F |
| 90 | F | T | T | T | T | T | T | T |
| 100 | F | T | T | T | T | T | T | T |
| 110 | F | T | T | T | T | T | T | T |
| 120 | F | T | T | T | T | T | T | T |
| 130 | F | T | T | T | T | T | T | T |
| 140 | F | T | T | T | T | T | T | T |
| 150 | F | T | T | T | T | T | T | T |
| 160 | F | T | T | T | T | T | T | T |
| 170 | F | T | T | T | T | T | T | T |
| 180 | F | T | T | T | T | T | T | T |
| 190 | F | T | T | T | T | T | T | T |
| 200 | F | T | T | T | T | T | T | T |

Table S2. Significance testing for Δnitrate. (T means statistically significant, and F means statistically non-significant)

| Depth (m) \ Time (Day) | t=-1 | t=0 | t=1 | t=2 | t=3 | t=5 | t=10 | t=15 |
|---|---|---|---|---|---|---|---|---|
| 0 | T | T | T | T | T | T | T | T |
| 10 | T | T | T | T | T | T | T | T |
| 20 | F | T | T | T | T | T | T | T |
| 30 | F | T | T | T | T | T | T | T |
| 40 | F | T | T | T | T | T | T | T |
| 50 | F | T | T | T | T | T | T | T |
| 60 | F | T | T | T | T | T | T | T |
| 70 | F | T | T | T | T | T | T | T |
| 80 | F | T | T | T | T | T | T | T |
| 90 | F | T | T | T | T | T | T | T |
| 100 | F | T | T | T | T | T | T | T |
| 110 | F | T | T | T | T | T | T | T |
| 120 | F | T | T | T | T | T | T | T |
| 130 | F | T | T | T | T | T | T | T |
| 140 | F | T | T | T | T | T | T | T |
| 150 | F | T | T | T | T | T | T | T |
| 160 | F | T | T | T | T | T | T | T |
| 170 | F | T | T | T | T | T | T | T |
| 180 | F | T | T | T | T | T | T | T |
| 190 | F | T | T | T | T | T | T | T |
| 200 | F | T | T | T | T | T | T | T |

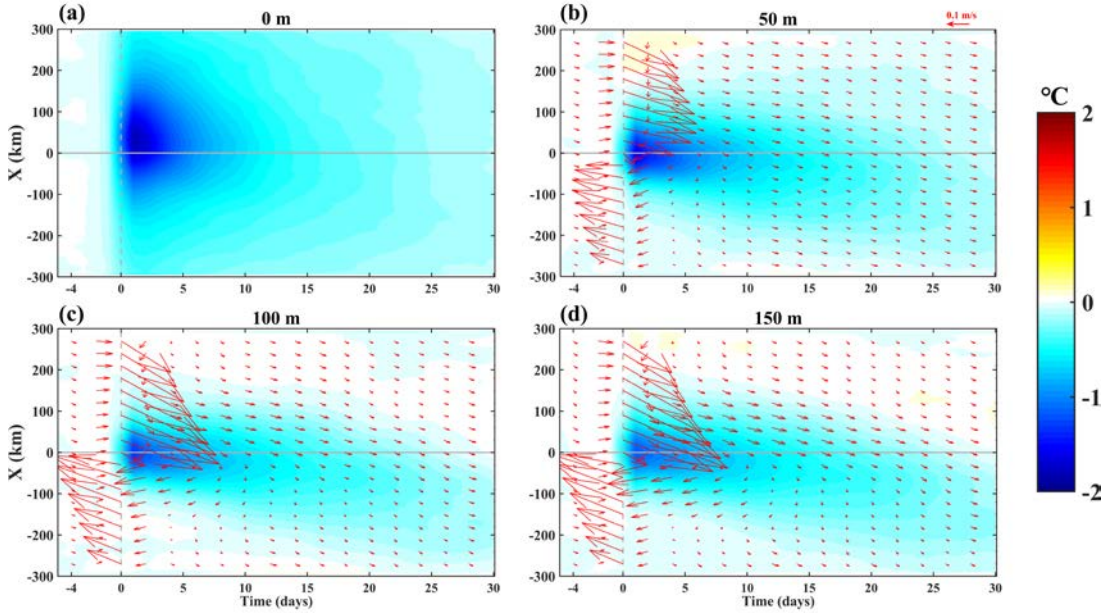


Figure S9. Temporal evolution of Δtemperature along the cross-track axis (Y=0) at 0, 50, 100, 150 m depths. The red arrows in b-d are the differences of currents between sea surface and corresponding depths (the latter minus the former). The gray dashed and solid lines in each panel denote the day of the TC passage and the position of the TC center, respectively.

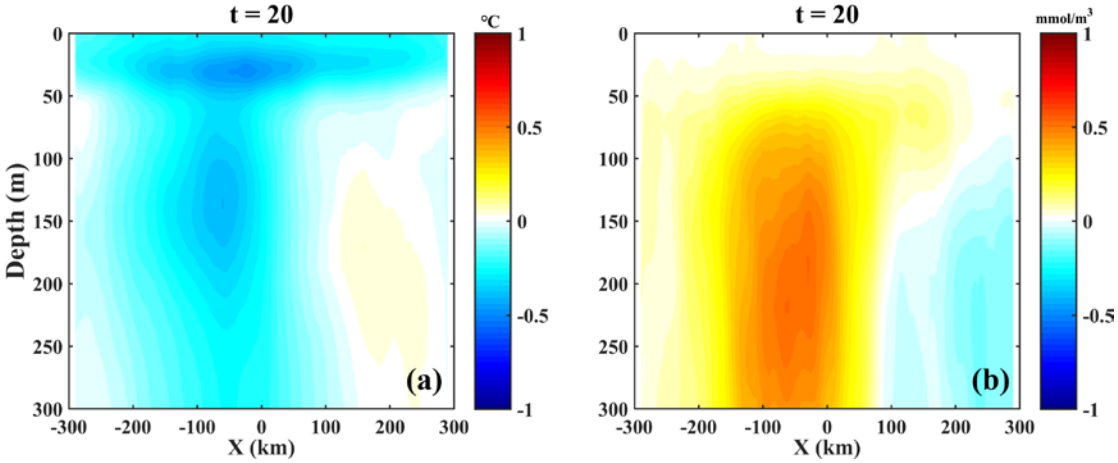


Figure S10. Vertical structures of (a) Δtemperature and (b) Δnitrate in the cross-track transect on the day 20 after the TC passage.

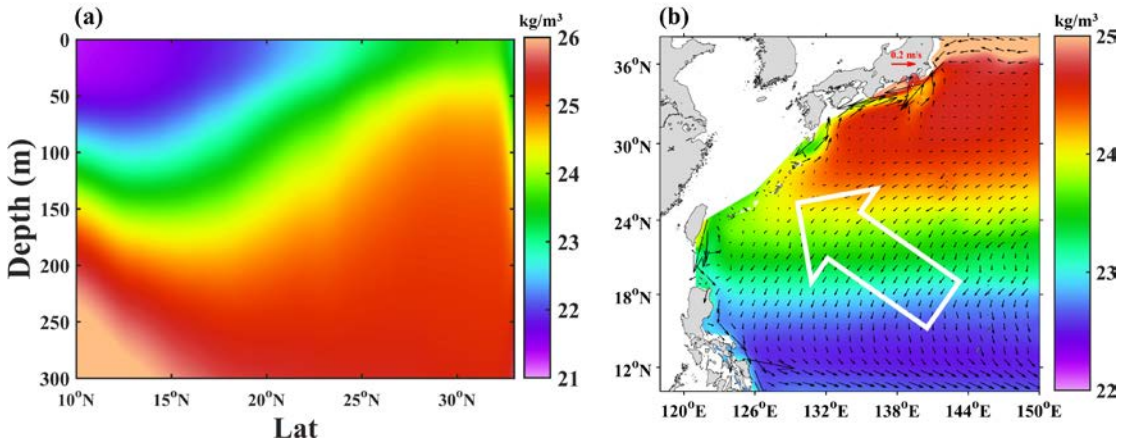


Figure S11. (a) Vertical structure of climatological mean σ along 135ºE. (b) Depth-averaged climatological mean σ above 200 m depth. The black arrows in b indicate the differences of currents between sea surface and 200 m depth (the latter minus the former). The white arrow in b represents the general moving direction of TCs in the Northwest Pacific.

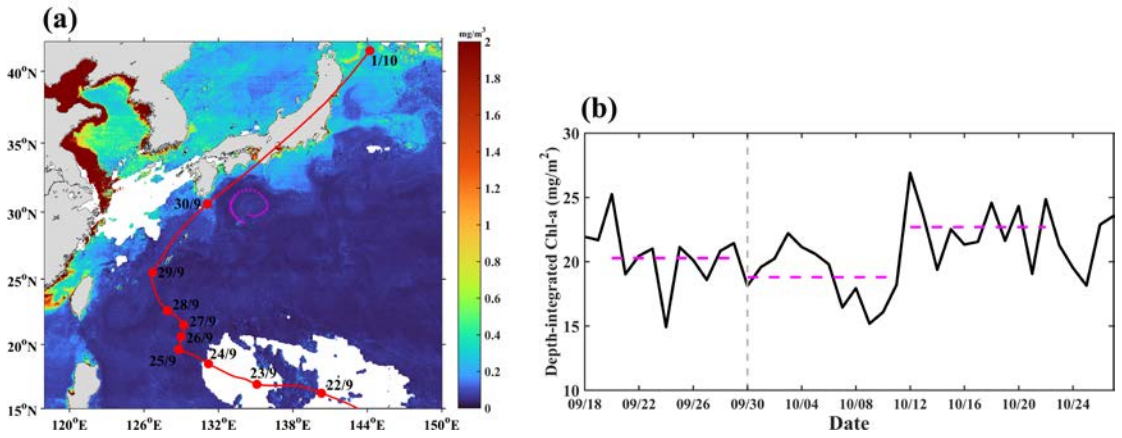


Figure S12. (a) The sea surface Chl-a field (shading) derived from Himawari-8 on September 23, 2018 in the northwestern Pacific. Red line with dots is the track of TC Trami. Magenta asterisks denote the positions of BGC-Argo 2902750 from September 18 to October 24. (b) Time series of depth-integrated Chl-a above 200 m depth observed by BGC-Argo 2902750. Gray dashed line denotes the day of TC Trami passage. Pink dashed lines are the mean values of depth-integrated Chl-a at different stages.